Amorphous molybdenum sulfide as highly efficient electron-cocatalyst for enhanced photocatalytic H$_2$ evolution

Huogen Yu [a,b,*], Pian Xiao [b], Ping Wang [b], Jiaguo Yu [c]

[a] State Key Laboratory of Silicate Materials for Architectures, Wuhan University of Technology, Wuhan 430070, People's Republic of China
[b] School of Chemistry, Chemical Engineering and Life Sciences, Wuhan University of Technology, Wuhan 430070, People's Republic of China
[c] State Key Laboratory of Advanced Technology for Material Synthesis and Processing, Wuhan University of Technology, Wuhan 430070, People's Republic of China

ARTICLE INFO

ABSTRACT

Exploiting novel and high-performance electron-cocatalysts without noble metallic element is of great significance for photocatalytic H$_2$-evolution reaction. Molybdenum sulfide is one of the promising candidates of such electron-cocatalysts, but its present performance is intrinsically restrained by the scarce active sites of unsaturated S atoms. In this study, amorphous MoS$_x$ (a-MoS$_x$) nanoparticles were directly anchored on the g-C$_3$N$_4$ surface by an adsorption-in situ transformation method with the aim of improving photocatalytic H$_2$-evolution activity. It was found that compared with the crystalline molybdenum sulfide (c-MoS$_2$), the a-MoS$_x$ cocatalyst clearly exhibited more unsaturated active S atoms due to its highly irregular arrangement structure. Photocatalytic experimental results suggested that the H$_2$-evolution activity of g-C$_3$N$_4$ photocatalyst could be obviously improved by loading a-MoS$_x$ cocatalyst, which is obviously higher than that of unmodified g-C$_3$N$_4$ and c-MoS$_2$/g-C$_3$N$_4$. More importantly, in addition to the g-C$_3$N$_4$, the amorphous MoS$_x$ could also work as the efficient electron cocatalyst to greatly enhance the photocatalytic performance of conventional H$_2$-evolution materials such as TiO$_2$ (a typical UV-light photocatalyst) and CdS (a typical Vis-light photocatalyst). On the basis of the present results, an electron-cocatalyst mechanism of amorphous MoS$_x$ was proposed to account for the improved photocatalytic H$_2$-evolution activity, namely, the amorphous MoS$_x$ can provide more unsaturated active S atoms as the efficient active sites to rapidly capture protons from solution, and then promote the direct reduction of H$^+$ to H$_2$ by photogenerated electrons. Considering its low cost and high efficiency, the amorphous MoS$_x$ cocatalyst would have great potential for the development of high-performance photocatalytic materials used in various fields.

1. Introduction

Hydrogen production by solar water splitting with semiconductor photocatalysts is believed to be one of the most attractive and promising solutions to global energy and environmental problems [1–3]. It is well known that the photocatalytic H$_2$-evolution performance for a photocatalyst heavily relies on the separation rate of photogenerated electron-hole pairs and their following interfacial catalytic reactions [4–6]. Unfortunately, it is usually impossible to develop a high-efficiency photocatalytic material only by using a single semiconductor due to the rapid recombination of elec-

trons and holes inside the photocatalyst or on its surface after light absorption. Therefore, various strategies such as coupling with other semiconductors [7,8], doping [9–11] and surface modification [12–15], have been widely utilized to improve their photocatalytic H$_2$-evolution activity. Among of them, electron-cocatalyst modification on a photocatalyst surface has been demonstrated to be one of the most efficient strategies for the enhanced photocatalytic performance via rapidly transferring interfacial electrons, retarding the recombination of photoexcited charges, and providing effective active sites [16–18]. The well-known electron-cocatalyst materials such as noble metals Pt, Ag and Pd have been extensively investigated and reported [19–21]. However, considering their expensive and scare properties, it is quite attracting and worthwhile to explore novel, inexpensive and earth-abundance electron cocatalysts to further improve the hydrogen-evolution performance. Indeed, extensive attempts by using non-noble metals (Co [22], Ni [23], and Fe [24,25]) or their oxides (Co$_3$O$_4$ [26], NiO [27] and Fe$_2$O$_3$

* Corresponding author at: State Key Laboratory of Silicate Materials for Architectures, Wuhan University of Technology, Wuhan 430070, People's Republic of China.
E-mail address: yuhuogen@whut.edu.cn (H. Yu).

[28]) as cost-effective electron cocatalysts have been widely investigated for enhanced photocatalytic H_2 generation. Yet it is still highly desirable and challenging to further develop new, low-cost and high-efficiency electron cocatalysts to satisfy the increasing demands for H_2 energy.

Molybdenum sulfide, a typically sheet-like transition metal sulfide, has attracted many attentions in various application fields such as dry lubrication [29], hydrodesulphurization reactions [30] and optical-electronic devices [31]. Recently, many reports indicated that molybdenum sulfide could function as an effective electron-cocatalyst in photocatalytic hydrogen-evolution reaction and even become a promising alternative to noble-metal catalysts [32,33]. For instance, Kanda et al. reported that the photocatalytic H_2 production performance of TiO_2 could be obviously improved by loading molybdenum sulfide nanoparticles [34]. Xiang et al. also indicted that the molybdenum sulfide modified rGO-TiO_2 composites exhibited an obviously higher hydrogen-production activity than the rGO-TiO_2 and TiO_2 [32]. According to the recent report by Chang et al. [35], the principal catalytic mechanism is that the unsaturated S atoms on the crystalline molybdenum sulfide edges can work as the efficient active sites to rapidly capture protons from solution, and then promote the direct reduction of H^+ to H_2 by photogenerated electrons. Hence, it is very significant and worthwhile to construct molybdenum sulfide cocatalyst with a large amount of unsaturated S atoms by optimizing its microstructure and morphology. More recently, Chang et al. further demonstrated that the photocatalytic performance of $nMoS_2/CdS$ (where n represents the layer numbers of MoS_2) had a significant increase with the gradually decreasing layer numbers of MoS_2, which was mainly attributed to the fact that the single or few layer MoS_2 had more unsaturated active S atoms [36]. Therefore, to further improve its electron-cocatalyst performance, the microstructure control of molybdenum sulfide with more unsaturated S atoms is highly required. Considering that the amorphous materials are in a highly irregular arrangement with many unsaturated or defect atoms compared with crystalline materials, it is expected that the amorphous molybdenum sulfide (MoS_x) modified photocatalysts should have a higher photocatalytic H_2 evolution activity. In fact, amorphous MoS_x has recently been demonstrated to be an excellent electrocatalyst working as the active centers for the H_2-evolution reaction [37,38]. On the basis of their similar mechanism of amorphous MoS_x for electron-catalytic and photocatalytic H_2 generation, it is expected that the amorphous MoS_x can be served as a highly efficient electron-cocatalyst for the enhanced photocatalytic H_2 evolution in various photocatalytic materials.

In this study, the amorphous MoS_x nanoparticles, as a new and highly efficient electron cocatalyst, have been successfully loaded on the g-C_3N_4 surface via an adsorption-in situ transformation method, namely, the initial electrostatic adsorption of MoS_4^{2-} ions on g-C_3N_4 surface and their subsequent in-situ self-transformation progress to form amorphous MoS_x cocatalyst. It was found that the photocatalytic activity of g-C_3N_4 photocatalyst could be obviously improved by loading amorphous MoS_x nanoparticle cocatalyst, which is obviously higher than that of well-known crystalline MoS_2 modified g-C_3N_4. More importantly, in addition to the g-C_3N_4, the amorphous MoS_x nanoparticles could also work as the efficient electron cocatalyst to greatly enhance the photocatalytic performance of conventional H_2-evolution materials such as TiO_2 (a typical UV-light responded photocatalyst) and CdS (a typical Vis-light responded photocatalyst). On the basis of the above experimental results, a possible electron-cocatalyst mechanism of amorphous MoS_x were proposed to account for the improved photocatalytic H_2-evolution activity of various photocatalytic materials. To the best of our knowledge, this is the first report about the amorphous MoS_x as a new, general and highly efficient electro-cocatalyst for the enhanced photocatalytic

H_2-evolution performance. Compared with the well-known noble metal electron-cocatalysts (such as Pt, Au, and Pd), the present amorphous MoS_x electron-cocatalyst could be considered to be one of the most promising H_2-evolution cocatalysts for the design and preparation of highly-efficiency photocatalytic materials in view of its facile synthesis, highly efficiency and low cost.

2. Experimental methods

2.1. Chemicals

Ammonium tetrathiomolybdate was purchased from Sigma Aldrich. Unless otherwise specified, all the other chemicals are analytical grade and supplied by Shanghai Chemical Reagent Ltd. (P.R. China) and used as received without further purification. Distilled water was used in all experiment.

2.2. Preparation of g-C_3N_4 photocatalyst

The g-C_3N_4 photocatalyst was obtained through a simple calcination-hydrothermal procedure by using melamine powder as the precursor. According to previous studies [2,8], the melamine precursor was calcined at 550 °C for 4 h in ambient atmosphere to obtain the bulk g-C_3N_4. To increase its specific surface area, the as-prepared g-C_3N_4 sample was further treated by a hydrothermal method. In briefly, 0.5 g of the calcined g-C_3N_4 powder was dispersed into 70 mL of deionized water, then stirred at room temperature for 1 h, and finally maintained at 180 °C for 12 h. After cooling down to room temperature, the resulting sample was washed for several times, and then dried at 60 °C for overnight to obtain the g-C_3N_4 photocatalyst.

2.3. Preparation of amorphous MoS_x-modified g-C_3N_4 photocatalyst

The amorphous MoS_x-modified g-C_3N_4 photocatalyst (a-MoS_x/g-C_3N_4) was synthesized via an adsorption-in situ transformation method. For a typical synthesis, the obtained g-C_3N_4 (0.2 g) powder was dispersed into 0.1 mol L^{-1} HCl solution (pH = 4), and then stirred at room temperature for 30 min to produce protonated g-C_3N_4 (g-C_3N_4/H^+). After that, 0.05 mol L^{-1} ammonium tetrathiomolybdate ((NH_4)$_2MoS_4$) was added into the above suspension solution and stirred for another 30 min to obtain MoS_4^{2-}-adsorbed g-C_3N_4/H^+ (g-C_3N_4/H^+-MoS_4^{2-}). Then, the resulting g-C_3N_4/H^+-MoS_4^{2-} suspension was maintained at 90 °C for 3 h under strongly stirring. After cooling naturally, the as-prepared sample was washed with distilled water for several times and dried at 60 °C for overnight to obtain a-MoS_x/g-C_3N_4 photocatalyst. In this study, the weight ratio of Mo to g-C_3N_4 was controlled to be 0.1, 0.5, 1, 3, and 5 wt%, and the corresponding samples can be denoted as a-MoS_x/g-C_3N_4 (Xwt%), where X refers to the weight ratio of Mo to g-C_3N_4.

2.4. Preparation of a-MoS_x/TiO_2 and a-MoS_x/CdS photocatalysts

The amorphous MoS_x-modified TiO_2 and CdS samples were also prepared under identical experimental conditions as the a-MoS_x/g-C_3N_4 by using TiO_2 and CdS as the precursors, respectively. In this case, the $W_{Mo}/W_{TiO2(orCdS)}$ is controlled to be 3 wt%, and the resulting samples can be denoted as a-MoS_x/TiO_2 (or a-MoS_x/CdS).

2.5. Preparation of the crystalline MoS_2-modified g-C_3N_4 photocatalyst

The crystalline MoS_2-modified g-C_3N_4 photocatalyst (c-MoS_2/g-C_3N_4) was prepared via an ultrasonic method by using

crystalline MoS_2 as the precursor [35]. For the preparation of crystalline MoS_2, 0.5 g of Na_2MoO_4 and 0.8 g of L-cysteine were dissolved in 80 mL of distilled water, and then maintained at 180 °C for 24 h. After washing by distilled water, the resulting crystalline MoS_2 (0.1 g) was dispersed into 100 mL of distilled water and sonicated for 2 h to prepare the black MoS_2 solution (1 mg/mL). For the synthesis of c-MoS_2/g-C_3N_4 sample, 0.2 g of the g-C_3N_4 was dispersed into 10 mL of crystalline MoS_2 solution (W_{Mo}/W_{g-C3N4} = 3 wt%) and then sonicated for 2 h. After washing with distilled water, the resultant sample was dried at 60 °C for 24 h to obtain the c-MoS_2/g-C_3N_4 photocatalyst.

2.6. Characterization

X-ray diffraction (XRD) was used to identify the crystal structures and phase compositions of the samples. Diffraction data were collected on a D/MAXRBX-ray diffractometer (Rigaku, Japan). X-ray photoelectron spectroscopy (XPS) measurements were done on a KRATOA XSAM800 XPS system with Mg Kα source. All the binding energies were referenced to the C1s peaks at 284.8 eV for the surface adventitious carbon. The morphology was observed by a JEM-7500F field emission scanning electronic microscopy (FESEM, JEOL, Japan). Further morphological and structural characterizations were based on transmission electron microscopy (TEM) and high-resolution transmission microscopy (HRTEM) observation using a JEM-2100F transmitting electron microscope. The Fourier transform infrared spectra (FTIR) were recorded using Nexus FTIR Spectrophotometer (Thermo Nicolet, America). UV–vis absorption spectra were obtained using a UV–vis spectrophotometer (UV-2450, Shimadzu, Japan). $BaSO_4$ was used as a reflectance standard in a UV–vis diffuse reflectance experiment. Photoluminescence spectra (PL) was measured at room temperature on a F-4500 fluorescence spectrophotometer (Japan, Hitachi) with an excitation wavelength of 365 nm.

2.7. Photocatalytic H_2 production activity

The photocatalytic H_2-generation reactions were carried out in a 100 mL three-necked Pyrex flask at ambient temperature and atmospheric pressure, and the outlets of the flask were sealed with a silicone rubber septum. The light source was four low-power LEDs (3 W, 420 nm, Shenzhen Lamplic Science Co. Ltd.). 50 mg of the photocatalytic powder was dispersed in 80 mL aqueous solution containing 10 vol% of lactic acid. Before each experiment, the system was bubbled with nitrogen for 30 min to remove the dissolved oxygen. In the process of irradiation, continuous stirring was applied to keep the photocatalyst particles in suspension state. Finally, hydrogen evolution was analyzed by a gas chromatograph (Shimadzu GC-1240, Japan, with nitrogen as a carrier gas) equipped with a 5 Å molecular sieve column and a thermal conductivity detector.

2.8. Photoelectrochemical measurements

Photoelectrochemical measurements and electrochemical impedance spectra (EIS) were performed on an electrochemical workstation (CHI660E) in a standard three-electrode configuration with a platinum wire as the counter electrode, saturated Hg/Hg_2Cl_2 (in saturated KCl) as a reference electrode, and Na_2SO_4 (0.5 M) aqueous solution as the electrolyte. The light source was provided by one 3-W LED (420 nm light source with a 90 mWcm^{-2} power or 365 nm light source with an 80 mWcm^{-2} power). The working electrodes were prepared on fluorine-doped tin oxide (FTO) conductor glass. Typically, the sample (10 mg) was ultrasonicated in 1 mL of anhydrous ethanol and 1 mL of Nafion D-520 dispersion (5%, w/w, in water and 1-propanol, Alfa Aesar) to disperse evenly
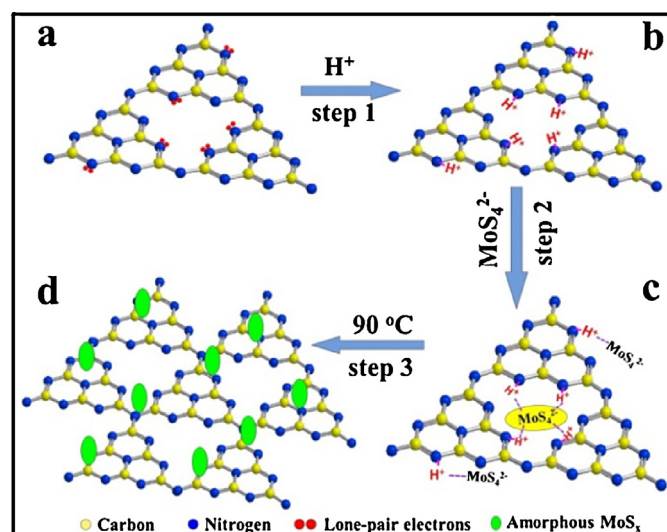
Fig. 1. Schematic illustration for the synthesis of a-MoS_x/g-C_3N_4 photocatalyst: (step 1) the protonation of (a) g-C_3N_4 to obtain (b) g-C_3N_4/H$^+$ in a HCl solution; (step 2) the electrostatic interaction between MoS_4^{2-} and g-C_3N_4/H$^+$ to obtain (c) g-C_3N_4/H$^+$-MoS_4^{2-}; (step 3) the in suit self-redox decomposition of MoS_4^{2-} on the g-C_3N_4 surface to produce (d) a-MoS_x/g-C_3N_4.

to obtain suspension solution. The suspension was spread on the FTO glass with the side protected by Scotch tape and dried at 60 °C for 12 h. A copper wire was connected to the side of the working electrode using conductive tape and the uncoated parts of the electrode were isolated with epoxy resin. Finally, the transient photocurrent responses with time (i–t curve) of the working electrodes were measured at a 0.5 V bias potential during repeated ON/OFF illumination cycles and EIS was determined over the frequency range of 0.01–10^5 Hz with an ac amplitude of 10 mV at the open circuit voltage.

3. Results and discussion

3.1. Synthesis and characterization of a-MoS_x/g-C_3N_4 photocatalyst

The synthetic procedure of a-MoS_x/g-C_3N_4 photocatalyst can be schematically illustrated through a facile adsorption-in situ transformation process, as shown in Fig. 1. Firstly, after the as-prepared g-C_3N_4 powder (Fig. 1a) is dispersed into a HCl solution for 30 min, the H$^+$ ions can be homogeneously and steadily adsorbed on the g-C_3N_4 surface to produce g-C_3N_4/H$^+$ suspension (Fig. 1b) as the N element with lone-pair electrons in the g-C_3N_4 can easily be protonated in an acid solution. In this case, when a $(NH_4)_2MoS_4$ solution is added into the above suspension solution, the g-C_3N_4/H$^+$ with high positive charges can attract MoS_4^{2-} ions to obtain the g-C_3N_4/H$^+$-MoS_4^{2-} suspension (Fig. 1c) via their strongly electrostatic interaction (step 2). As a consequence, a tightly coupling interaction between the g-C_3N_4 and MoS_4^{2-} was subsequently formed. Finally, a following low-temperature treatment at 90 °C (step 3) can cause the in situ self-transformation of MoS_4^{2-} precursor into amorphous MoS_x on the g-C_3N_4 surface, thus producing the a-MoS_x/g-C_3N_4 photocatalyst (Fig. 1d). Considering the fact that the MoS_4^{2-} ions can be homogeneously and strongly coupled on the whole g-C_3N_4 surface via the uniformly protonated N element, it is reasonable to deduce that the resultant amorphous MoS_x cocatalyst can be well dispersed on the g-C_3N_4 surface to form a-MoS_x/g-C_3N_4 photocatalyst.

To demonstrate the successful loading of amorphous MoS_x phase on the g-C_3N_4 surface, the a-MoS_x/g-C_3N_4 photocatalyst is
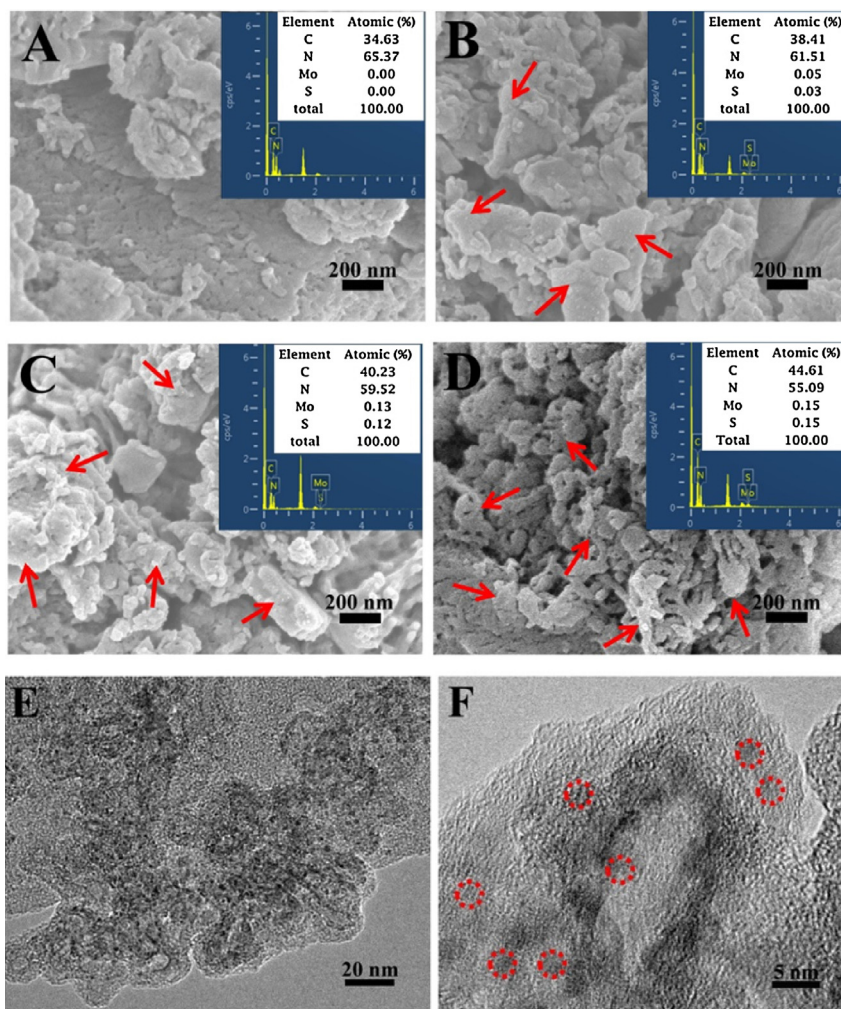
Fig. 2. FESEM images of various samples: (A) g-C_3N_4, (B) a-MoS_x/g-C_3N_4(1 wt%), (C) a-MoS_x/g-C_3N_4(3 wt%), and (D) a-MoS_x/g-C_3N_4(5 wt%); (E,F) HRTEM images of a-MoS_x/g-C_3N_4(3 wt%).

firstly characterized by FESEM and HRTEM (Fig. 2). It can be seen that the morphology of g-C_3N_4 sample is in an irregular structure with many disordered nano-pores (Fig. 2A), which was produced during the high-temperature calcination of melamine. After the g-C_3N_4 surface is modified with molybdenum sulfide cocatalyst, the resulting a-MoS_x/g-C_3N_4 (Figs. 2B–D) samples exhibit a similar morphology with the g-C_3N_4 sample owning to a mild modification process. However, further observation indicates that many small nanoparticles (show in the red arrow) are homogeneously distributed on the g-C_3N_4 surface, and with increasing amount of $(NH_4)_2MoS_4$, more nanoparticles are produced owning to the adsorption of more MoS_4^{2-} precursor on the g-C_3N_4 surface. According to their EDX results, the above small nanoparticles can be ascribed to molybdenum sulfide in view of the presence of characteristic Mo and S peaks in addition to the main C and N elements. In addition, the amount of molybdenum in the a-MoS_x/g-C_3N_4 samples gradually increased from ca. 0.05–0.15 at% with increasing weight ratio of Mo from 1 to 5 wt%. To further observe the morphology and phase structure of the molybdenum sulfide nanoparticles, their corresponding TEM images are shown in Figs. 2E and F. It is clear that the molybdenum sulfide nanoparticles (the black dots in the range of 2–4 nm) are homogeneously dispersed on the g-C_3N_4 surface, in good agreement with the FESEM results. The high-resolution TEM image of a-MoS_x/g-C_3N_4(3 wt%) indicates that those molybdenum sulfide nanoparticles are in amorphous phase (no lattice fringes can be
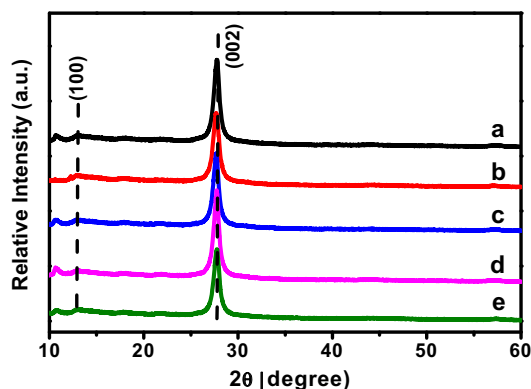
Fig. 3. XRD patterns of various samples: (a) g-C_3N_4, (b) a-MoS_x/g-C_3N_4(0.1 wt%), (c) a-MoS_x/g-C_3N_4(1 wt%), (d) a-MoS_x/g-C_3N_4(3 wt%), and (e) a-MoS_x/g-C_3N_4(5 wt%).

found) owning to a low-temperature preparation method. Therefore, the above results strongly demonstrated that the amorphous MoS_x nanoparticles have been successfully and homogeneously loaded on the g-C_3N_4 surface to form a-MoS_x/g-C_3N_4 photocatalyst by the facile adsorption-in situ transformation method.

The phase structure of amorphous MoS_x on the g-C_3N_4 surface can further be revealed by XRD results, as show in Fig. 3. It is found that all the diffraction peaks of
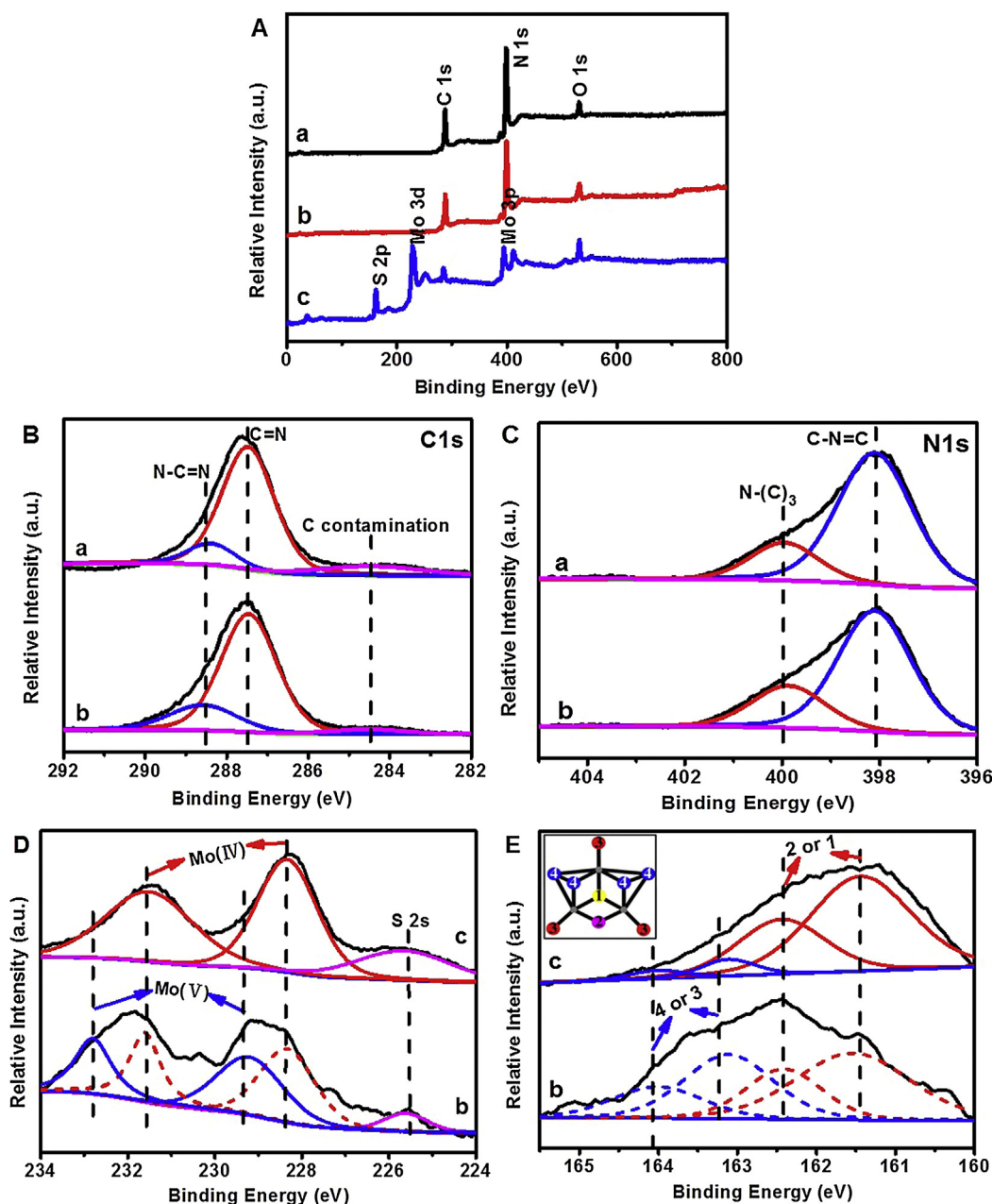
Fig. 4. Typical (A) XPS survey spectra and high-resolution XPS spectra of (B) C 1s, (C) N 1s, (D) Mo 3d and (E) S 2p for various samples: (a) g-C_3N_4, (b) a-MoS$_x$/g-C_3N_4(3 wt%) and (c) crystalline MoS_2. Inset in Fig. 4E showing the possible chemical states of S element in MoS$_x$: (1) saturated basal-plane S atom with three-coordination bonds to Mo atoms; (2) unsaturated terminal S atom with two-coordination bonds to Mo; (3) unsaturated apical S atom with one-coordination bond to Mo; and (4) unsaturated bridging S atom with one persulfide ligand.

g-C_3N_4 and a-MoS$_x$/g-C_3N_4 samples are indexed to be g-C_3N_4 phase (JCPDS 87–1526). Moreover, no obvious change about the diffraction-peak intensity and full width at half-maximum of the a-MoS$_x$/g-C_3N_4 photocatalyst can be found compared with the pure g-C_3N_4 sample, revealing that the crystal structure of g-C_3N_4 photocatalyst cannot be effected by the facile surface modification of amorphous MoS$_x$ cocatalyst, in good agreement with the FESEM results. Significantly, no characteristic diffraction peaks about the molybdenum sulfide phases [14,39,40] can be found in the a-MoS$_x$/g-C_3N_4 photocatalyst, indicating that the molybdenum sulfide cocatalyst is in amorphous structure as a result of the low-temperature synthesis, which can clearly be seen in the HRTEM image (Fig. 2F). The surface microstructures of amorphous MoS$_x$ on the g-C_3N_4 surface can further be characterized by XPS results.

Fig. 4A shows the typical XPS survey spectra of g-C_3N_4 before and after modification by amorphous MoS$_x$ cocatalyst. It is clear that all the prepared samples show the main XPS peaks of carbon and nitrogen elements, which are mainly from the g-C_3N_4 phase [39,41,42]. Their high-resolution XPS results exhibit that all the samples show a similar binding energy for the C 1s (Fig. 4B) and N 1s elements (Fig. 4C), suggesting that the surface loading of amorphous MoS$_x$ shows no effect on the chemical states of the g-C_3N_4 photocatalyst due to a low-temperature modification progress, in good agreement with the XRD and FESEM results. In addition, a low-intensity XPS peak of O element can be observed in the survey spectra (Fig. 4A), which can be contributed to the H_2O or −OH adsorbed on the photocatalyst surface during the aqueous-route preparation.
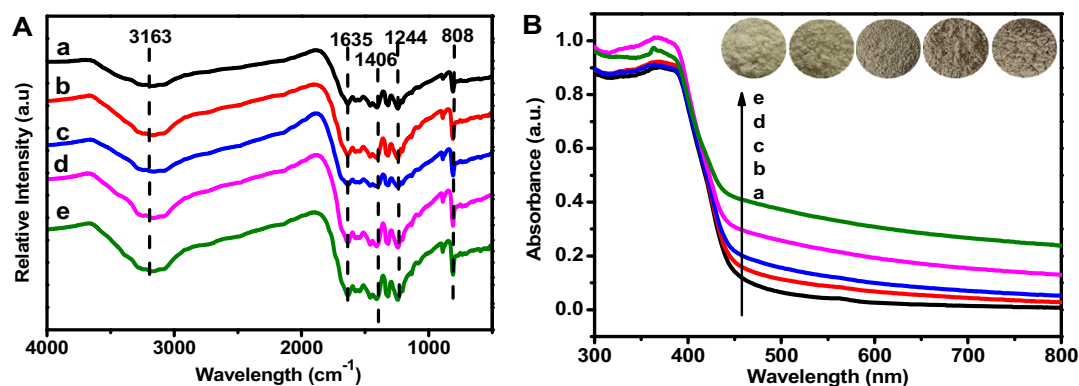
Fig. 5. (A) FTIR spectra, (B) UV–vis spectra and (inset) the corresponding photographs for various samples: (a) g-C$_3$N$_4$, (b) a-MoS$_x$/g-C$_3$N$_4$(0.1 wt%), (c) a-MoS$_x$/g-C$_3$N$_4$(1 wt%), (d) a-MoS$_x$/g-C$_3$N$_4$(3 wt%), and (e) a-MoS$_x$/g-C$_3$N$_4$(5 wt%).

Considering a very limited amount of amorphous MoS$_x$ cocatalyst on the g-C$_3$N$_4$ surface, the XPS peaks about the amorphous MoS$_x$ cannot be easily observed in the XPS survey spectra. In this case, the high-resolution XPS peaks about Mo and S elements are employed to further investigate its chemical states (Figs. 4D and E). For comparison, the crystalline MoS$_2$ sample was also tested under an identical condition. It is very clear that the XPS Mo 3d spectrum of crystalline molybdenum sulfides shows two individual peaks at ca. 228.34 and 231.58 eV (Fig. 4D–c), which can be assigned to Mo 3d$_{5/2}$ and Mo 3d$_{3/2}$ peaks for Mo^{4+} ions [32,43], respectively. However, the amorphous MoS$_x$ shows a quite different Mo 3d spectrum with a broader binding-energy values compared with the crystalline MoS$_2$ (Fig. 4D–b), which can be mainly divided into four peaks in addition to the co-existence of S 2s peak (ca. 225.5 eV). It is found that in addition to the Mo^{4+} ions, the higher binding energies at 232.82 and 229.35 eV can be well attributed to the Mo^{5+} ions [37,38,44–46], which clearly reveals that the chemical state of Mo element in the amorphous MoS$_x$ are mainly composed of +4 and +5. The corresponding S 2p spectrum can provide further information about the microstructures of amorphous MoS$_x$ cocatalyst, as show in Fig. 4E. It has been reported that there are four kinds of S-bonding configurations existing in the molybdenum sulfide materials [38,45,47], including one kind of saturated basal-plane S atom (the yellow S-(1)) with three-coordination bonds to Mo atoms and three kinds of unsaturated S atoms such as the terminal S^{2-} (the pink S-(2)) with two-coordination bonds to Mo atoms, the apical S^{2-} (the red S-(3)) with one-coordination bond to Mo atom and the bridging S$_2$$^{2-}$ (the blue S-(4)) with one persulfide ligand, as shown in the inset of Fig. 4E. In addition, it has been reported that the saturated basal-plane S and unsaturated terminal S atoms show a comparable binding energy, while the unsaturated apical S and bridging S atoms exhibit an analogous binding energy [37]. For the crystalline molybdenum sulfides, the S element usually exhibits two XPS peaks at ca. 161.54 and 162.41 eV (Fig. 4E–c), which is mainly attributed to the saturated basal-plane S atom (the yellow S-(1)) in view of its perfect crystalline structure. In fact, in addition to the main saturated S atoms, a small amount of unsaturated S atoms such as apical S^{2-} and bridging S$_2$$^{2-}$ can also be found, which comes from the surface of crystalline molybdenum sulfide nanoparticles. For the present a-MoS$_x$/g-C$_3$N$_4$ sample, it shows a very broad S 2p peak with a binding energy range from 160 to 165.5 eV, which is completely different from the above results of crystalline molybdenum sulfides. By curve-fitting with a Gaussian–Lorentzian method, it is found that the characteristic peaks located at 161.54 (peak 1) and 162.41 eV (peak 2) can correspond to the saturated basal-plane S and the unsaturated terminal S atoms, while the higher binding energies at 163.11 (peak 3) and 164.01 eV (peak 4) are primarily from the unsaturated apical S and bridging S atoms [37,38]. Consid-

ering the highly irregular arrangement with many unsaturated or defect atoms in amorphous molybdenum sulfides compared with crystalline sample, it is deduced that the above peaks (1) and (2) can be mainly ascribed to the unsaturated terminal S atom in the a-MoS$_x$/g-C$_3$N$_4$ photocatalysts. According to the element analysis based on the XPS results, the stoichiometric ratio of S to Mo in the amorphous MoS$_x$ can be calculated to be 3.3:1, which clearly suggests that the S atoms are primarily located on the a-MoS$_x$ surface. Therefore, the above results strongly demonstrated that the amorphous MoS$_x$ nanoparticles with many unsaturated S atoms have been successfully loaded on the surface of g-C$_3$N$_4$ photocatalyst.

FTIR and UV–vis spectra can provide further information about the successful loading of amorphous MoS$_x$ on the g-C$_3$N$_4$ photocatalyst surface. Fig. 5A shows the FTIR spectra of pure g-C$_3$N$_4$ and a-MoS$_x$/g-C$_3$N$_4$ photocatalysts. It is clear that all the samples shows many obvious absorption peaks corresponding to various vibration modes, such as the tri-s-triazine structure (808 cm^{-1}), heptazine heterocycles (1635, 1406, 1244 cm^{-1}) and the un-reacted amino group (3100–3300 cm^{-1}), which can be attributed to the typical groups in g-C$_3$N$_4$ photocatalysts. As for the a-MoS$_x$/g-C$_3$N$_4$ samples, no obvious change for the characteristic absorption peaks can be observed compared with the g-C$_3$N$_4$, which is in high accordance with the FESEM, XRD and XPS results. Considering a very limited amount of amorphous MoS$_x$, no related absorption peaks of amorphous MoS$_x$ can be detected. Fig. 5B shows the UV–vis spectra of pure g-C$_3$N$_4$ and a-MoS$_x$/g-C$_3$N$_4$ photocatalysts. It is found that the g-C$_3$N$_4$ sample only shows the band-gap absorption at ca. 450 nm, corresponding to a band gap of ca. 2.8 eV. After surface loading of amorphous MoS$_x$ nanoparticles, the resultant a-MoS$_x$/g-C$_3$N$_4$ samples show a wide visible-light absorption in the range of 450–800 nm in addition to the band-gap absorption of g-C$_3$N$_4$. Moreover, with increasing amount of the amorphous MoS$_x$ cocatalyst, there is a gradually increased absorption in the visible-light range for the a-MoS$_x$/g-C$_3$N$_4$ photocatalysts, which clearly suggests the formation of more amorphous MoS$_x$ on the g-C$_3$N$_4$ surface, in good agreement with their corresponding color change from yellow to brown (the inset of Fig. 5B).

3.2. Photocatalytic performance and mechanism

The photocatalytic performances of various samples were evaluated by detecting the hydrogen evolution under visible light, as shown in Fig. 6A. For comparison, the crystalline MoS$_2$-modified g-C$_3$N$_4$ photocatalyst (c-MoS$_2$/g-C$_3$N$_4$) was prepared via an ultrasonic method by using crystalline MoS$_2$ as the precursor and its photocatalytic activity was tested under an identical experimental condition. It can be seen that the pure g-C$_3$N$_4$ photocatalyst shows a negligible photocatalytic H$_2$-evolution activity
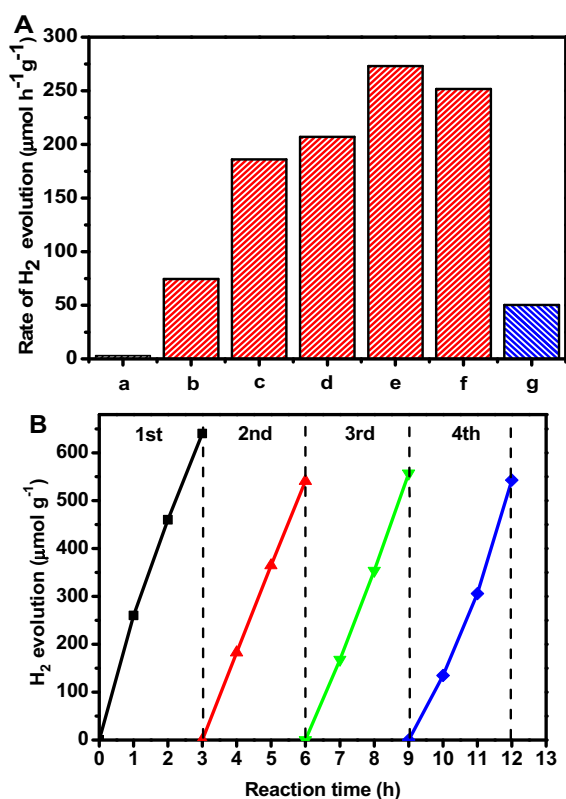
Fig. 6. (A) Photocatalytic H_2-evolution activities of various samples: (a) g-C_3N_4, (b) a-MoS$_x$/g-C_3N_4(0.1 wt%), (c) a-MoS$_x$/g-C_3N_4(0.5 wt%), (d) a-MoS$_x$/g-C_3N_4(1 wt%), (e) a-MoS$_x$/g-C_3N_4(3 wt%), (f) a-MoS$_x$/g-C_3N_4(5 wt%), and (g) c-MoS$_2$/g-C_3N_4(3 wt%); (B) cycling runs for the photocatalytic H_2 evolution of a-MoS$_x$/g-C_3N_4(3.0 wt%) photocatalyst.

Fig. 7. The photocatalytic performance (A) and transient photocurrent responses (B) of typical photocatalytic materials before and after a-MoS$_x$ modification: (a) g-C_3N_4, (a′) a-MoS$_x$/g-C_3N_4 (3.0 wt%); (b) TiO$_2$, (b′) a-MoS$_x$/TiO$_2$(3.0 wt%); (c) CdS, (c′) a-MoS$_x$/CdS (3.0 wt%).

(ca. 3.0 μmol h^{-1} g^{-1}) due to the absence of highly efficient electron cocatalysts, in good agreement with the reported results [7,8]. When the amorphous MoS$_x$ cocatalyst is modified on the g-C_3N_4 surface, all the resultant a-MoS$_x$/g-C_3N_4 samples exhibit a remarkably higher photocatalytic H_2-evolution activity than the pure g-C_3N_4. Especially, when the amount of Mo element is controlled to be 3 wt%, the obtained a-MoS$_x$/g-C_3N_4(3 wt%) photocatalyst achieves the highest photocatalytic performance with a H_2-production rate of 273.1 μmol h^{-1} g^{-1}, which is obviously higher than that of pure g-C_3N_4 by a factor of 91.03 times. However, further increase of the amount of a-MoS$_x$ cocatalyst results in a slightly decreased photocatalytic activity, in good agreement with other cocatalyst-modified photocatalysts (such as Fe(III)/AgBr [48], Cu(II)/AgBr [49] and Cu(II)/TiO$_2$ [50]). On the other hand, compared with the well-known c-MoS$_2$/g-C_3N_4 photocatalyst with a H_2-production rate of 50.36 μmol h^{-1} g^{-1}, all of the amorphous MoS$_x$-modified g-C_3N_4 samples show an obviously higher photocatalytic H_2-production performance.

To further evaluate the performance stability of the a-MoS$_x$/g-C_3N_4 photocatalyst, a recycling test (Fig. 6B) and the effect of pH value (Fig. S1) on the photocatalytic H_2 evolution activity of the a-MoS$_x$/g-C_3N_4(3 wt%) sample is performed. Fig. 6B shows a recycling test of a-MoS$_x$/g-C_3N_4(3 wt%) photocatalyst. It is very clear that the a-MoS$_x$/g-C_3N_4(3 wt%) photocatalyst can maintain a stable and effective photocatalytic performance. Moreover, the effect of pH value on the photocatalytic H_2 evolution activity of a-MoS$_x$/g-C_3N_4(3.0 wt%) has been carefully investigated and the corresponding results were shown as follows (Fig. S1). It was found that the a-MoSx/g-C_3N_4 can exhibit a high photocatalytic performance in a wide pH range of 1.66–4.80.
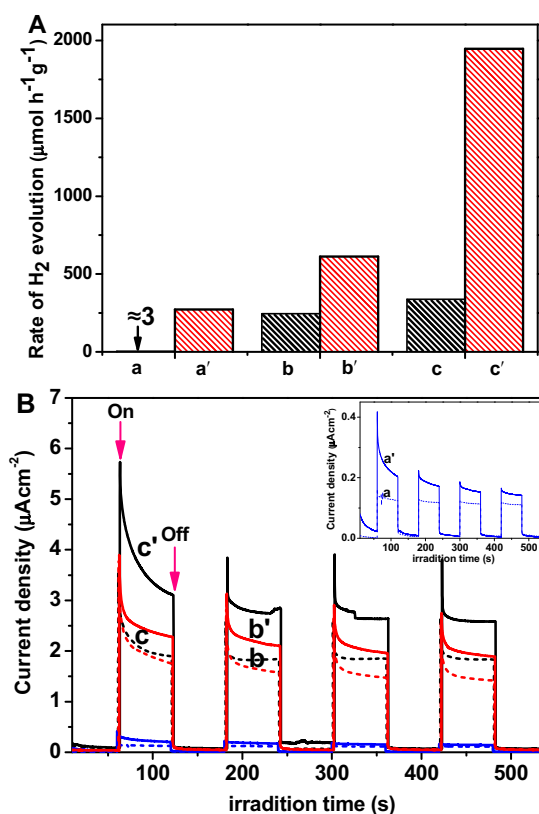
As a highly efficient cocatalyst for photocatalytic materials, it is very interesting and worthwhile to investigate that whether the amorphous MoS$_x$ cocatalyst can work as a general cocatalyst to greatly improve the photocatalytic performance of various photocatalysts. In addition to the g-C_3N_4, the conventional H_2-evolution materials such as TiO$_2$ (a typical UV-light responded photocatalyst) and CdS (a typical Vis-light responded photocatalyst) are also modified with the amorphous MoS$_x$ nanoparticle cocatalyst under an identical experimental conditions as the a-MoS$_x$/g-C_3N_4 and their corresponding photocatalytic performance is investigated before and after surface modification by amorphous MoS$_x$ cocatalyst, as shown in Fig. 7A. It is clear that all of the amorphous MoS$_x$ modified samples show an obviously enhanced photocatalytic H_2-evolution performance compared with their corresponding unmodified samples. To further understand the role of amorphous MoS$_x$ cocatalyst in photocatalytic H_2-evolution reaction, the transient photocurrent responses of those samples are also investigated (Fig. 7B). It can be found that all of the amorphous MoS$_x$ loaded photocatalysts exhibit a higher transient photocurrent density than their corresponding unmodified samples, strongly suggesting an obviously enhanced separation efficiency of photogenerated electron–hole pairs by the amorphous MoS$_x$ cocatalyst, in good agreement with the results in Fig. 7A. Therefore, the above results definitely verify that amorphous MoS$_x$ cocatalyst can become a novel, effective, and general cocatalyst to greatly improve the photocatalytic H_2-evolution performance of photocatalytic materials.

On the basis of the above results, it can be concluded that amorphous MoS$_x$ has an important effect on the enhanced photocatalytic H_2-evolution activity of various photocatalytic materials. To clearly investigate the improved photocatalytic performance of amorphous MoS$_x$-modified photocatalyst, a possible photo-
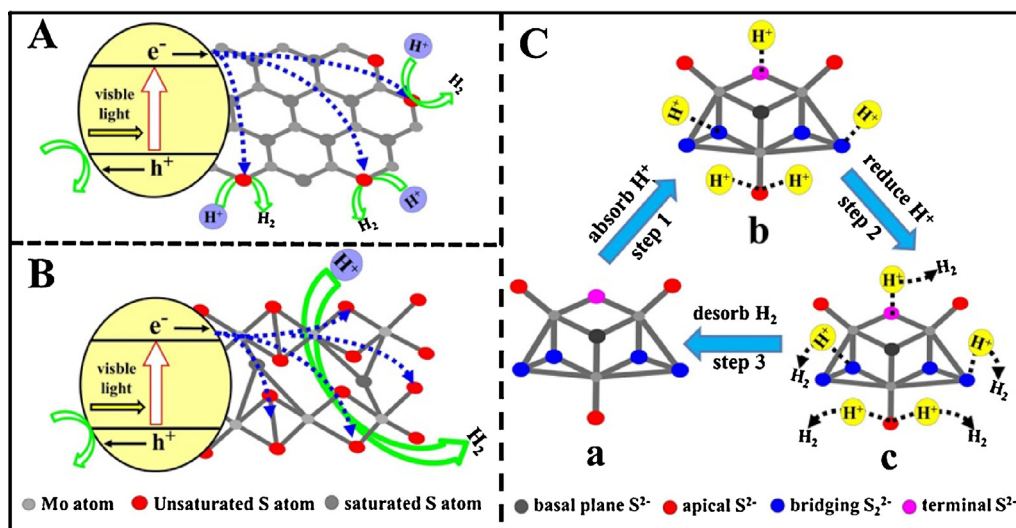
Fig. 8. Schematic diagram illustrating the photocatalytic H_2-evolution mechanism: (A) c-MoS_2-modified photocatalyst, (B) a-MoS_x-modified photocatalyst; and (C) the microstructure change of amorphous MoS_x cocatalyst in (B) during photocatalytic H_2 evolution.

catalytic mechanism of amorphous MoS_x as the highly efficient electron cocatalyst was proposed and shown in Fig. 8. It has been widely reported that the crystalline molybdenum sulfide is an effective electron-cocatalyst for the hydrogen-evolution reaction [32,35]. The enhanced photocatalytic mechanism can be well explained by the fact that the unsaturated S atoms on the crystalline molybdenum sulfide surface work as the efficient active sites to rapidly capture protons from solution, and then promote the direct reduction of H^+ to H_2 by photogenerated electrons (Fig. 8A). However, considering a very limited number of unsaturated active S atoms on the crystalline molybdenum sulfide surface, it is easy to deduce that the H_2-evolution performance of c-MoS_x/g-C_3N_4 is still very low (Fig. 6A). For the amorphous molybdenum sulfide nanoparticle as the electron cocatalyst, the unsaturated S atoms not only locate on the nanoparticle surface, but also widely exist in the whole MoS_x nanoparticles (Fig. 4E). As a result, compared with the widely reported crystalline molybdenum sulfide (the active sites only existing on the edges or surface), one of the most obvious advantages is that the whole amorphous MoS_x nanoparticle can function as the effective H_2-evolution active center to rapidly promote the interfacial catalytic reactions (Fig. 8B). To further explain the possible microstructure change of the amorphous MoS_x during photocatalytic H_2-evolution reaction, a schematic illustration for the photocatalytic mechanism is shown in Fig. 8C. According to the above XPS analysis and the previously reported results [37,38], the amorphous MoS_x is mainly composed of three kinds of unsaturated S atoms including the terminal S^{2-}, apical S^{2-} and bridging S_2^{2-} (Fig. 8C–a). Considering the different unsaturated configurations of S atoms in the amorphous MoS_x structure, it is believed that the different S-atom configuration shows different H^+-adsorption ability in the reaction system. Obviously, the apical S^{2-} is from the S atom with monocoordination structure and can capture a couple of H^+ ions, while the terminal S^{2-} and bridging S_2^{2-} can only absorb one H^+ ion owing to their two-coordination structure (Fig. 8C–b). After the inject of photogenerated electrons into the amorphous MoS_x cocatalyst, the adsorbed H^+ ions on the unsaturated S active sites can rapidly be reduced to release H_2 (Fig. 8C–c). In addition, the present very small size (2–4 nm in Fig. 2) is very beneficial not only to the effective diffusion and adsorption of H^+ ions on the whole amorphous MoS_x cocatalyst, but also to the rapid capture of photogenerated electrons by adsorbed H^+ ions due to its very short transportation route. Therefore, owing to the repeating adsorption-desorption of H^+ ions on the whole amorphous MoS_x nanoparticles,

the resultant a-MoS_x/g-C_3N_4 photocatalysts show a highly effective and stable photocatalytic H_2-evolution performance.

The improved photocatalytic performance of the a-MoS_x/g-C_3N_4 photocatalyst can be further demonstrated by the rapid charge transfer and separation via the PL spectra and electrochemical impedance spectra (EIS). Fig. S2 and Fig. S3 show the PL spectra and EIS for the a-MoS_x/g-C_3N_4 photocatalyst, respectively. It can be found that a strong PL emission peak of all samples is observed at about 435 nm, which can be attributed to the recombination of photo-induced electrons and holes for g-C_3N_4. Moreover, the emission-peak intensity of the a-MoS_x/g-C_3N_4 photocatalyst gradually decreased with the increase of Mo amounts, indicating a lower recombination possibility of photogenerated charge carriers than naked g-C_3N_4. On the other hand, it can be seen that the arc radius on the EIS plots of all the a-MoS_x/g-C_3N_4 was smaller than that of g-C_3N_4 under visible light, suggesting a smaller charge transfer resistance on the electrode surface for a-MoS_x/g-C_3N_4 photocatalyst [42]. Especially, when the amount of Mo element is controlled to be 3 wt%, there is the smallest arc radius on the EIS plots for the a-MoS_x/g-C_3N_4(3 wt%) photocatalyst, suggesting the highest efficiency of photoinduced electron-hole pairs through an interfacial interaction between g-C_3N_4 and a-MoS_x nanoparticles.

4. Conclusions

In summary, the amorphous MoS_x nanoparticles were directly loaded on the g-C_3N_4 surface by an adsorption-in situ transformation method, namely, the initial electrostatic adsorption of MoS_4^{2-} ions on g-C_3N_4 surface and their subsequent in-situ self-transformation progress to form amorphous MoS_x cocatalyst. It was found that the resultant a-MoS_x/g-C_3N_4 photocatalysts displayed markedly higher photocatalytic H_2-evolution activities than the unmodified g-C_3N_4 and crystalline MoS_2-modified g-C_3N_4. Significantly, in addition to the g-C_3N_4, the amorphous MoS_x could also be used as an effective electron cocatalyst to greatly improve the H_2-evolution activity of the conventional photocatalytic materials such as TiO_2 and CdS. On the basis of the present results, an electron-cocatalyst mechanism of amorphous MoS_x was proposed to account for the improved photocatalytic H_2-evolution activity, namely, the amorphous MoS_x can provide more unsaturated active S atoms as the efficient active sites to rapidly capture protons from solution, and then promote the direct reduction of H^+ to H_2 by photogenerated electrons. Considering its low cost and high efficiency,

the amorphous MoS$_x$ cocatalyst would have great potential for the development of high-performance photocatalytic materials.

Acknowledgements

Appendix A. Supplementary data

Supplementary data associated with this article can be found, in the online version, at http://dx.doi.org/10.1016/j.apcatb.2016.04.028.

References

[1] S. Linic, P. Christopher, D.B. Ingram, Nat. Mater. 10 (2011) 911–921.
[2] S. Cao, J. Low, J. Yu, M. Jaroniec, Adv. Mater. 27 (2015) 2150–2176.
[3] J. Song, Z.-F. Huang, L. Pan, J. Zou, X. Zhang, L. Wang, ACS Catal. 5 (2015) 6594–6599.
[4] H. Yu, W. Chen, X. Wang, Y. Xu, J. Yu, Appl. Catal. B: Environ. 187 (2016) 163–170.
[5] M.K. Bhunia, S. Melissen, M.R. Parida, P. Sarawade, J.M. Basset, D.H. Anjum, O.F. Mohammed, P. Sautet, T. Le Bahers, K. Takanabe, Chem. Mater. 27 (2015) 8237–8247.
[6] J. Schneider, M. Matsuoka, M. Takeuchi, J. Zhang, Y. Horiuchi, M. Anpo, D. Bahnemann, Chem. Rev. 114 (2014) 9919–9986.
[7] H. Shi, G. Chen, C. Zhang, Z. Zou, ACS Catal. 4 (2014) 3637–3643.
[8] H. Yu, F. Chen, F. Chen, X. Wang, Appl. Surf. Sci. 358 (2015) 385–392.
[9] Z. Huang, J. Song, L. Pan, Z. Wang, X. Zhang, J. Zou, W. Mi, X. Zhang, L. Wang, Nano Energy. 12 (2015) 646–656.
[10] J. Wang, P. Zhang, X. Li, J. Zhu, H. Li, Appl. Catal. B: Environ. 134 (2013) 198–204.
[11] X. Ding, W. Ho, J. Shang, L. Zhang, Appl. Catal. B: Environ. 182 (2016) 316–325.
[12] H. Tada, Q. Jin, H. Nishijima, H. Yamamoto, M. Fujishima, S. Okuoka, T. Hattori, Y. Sumida, H. Kobayashi, Angew. Chem. Int. Ed. 123 (2011) 3563–3567.
[13] M. Miyauchi, H. Irie, M. Liu, X. Qiu, H. Yu, K. Sunada, K. Hashimoto, J. Phys. Chem. Lett. 7 (2016) 75–84.
[14] H. Yu, G. Cao, F. Chen, X. Wang, J. Yu, M. Lei, Appl. Catal. B: Environ. 160–161 (2014) 658–665.
[15] D. Zhang, M. Wen, S. Zhang, P. Liu, W. Zhu, G. Li, H. Li, Appl. Catal. B: Environ. 147 (2014) 610–616.
[16] R. Li, F. Zhang, D. Wang, J. Yang, M. Li, J. Zhu, X. Zhou, H. Han, C. Li, Nat. Commun. 4 (2013) 1432.
[17] H. Yu, J. Tian, F. Chen, P. Wang, X. Wang, Sci. Rep. 5 (2015) 13083.
[18] Y. Xu, Y. Mo, J. Tian, P. Wang, H. Yu, J. Yu, Appl. Catal. B: Environ. 181 (2016) 810–817.
[19] Q. Zhai, S. Xie, W. Fan, Q. Zhang, Y. Wang, W. Deng, Y. Wang, Angew. Chem. Int. Ed. 125 (2013) 5888–5891.
[20] H. Yu, R. Liu, X. Wang, P. Wang, J. Yu, Appl. Catal. B: Environ. 111–112 (2012) 326–333.
[21] R. Liu, P. Wang, X. Wang, H. Yu, J. Yu, J. Phys. Chem. C 116 (2012) 17721–17728.
[22] Y. Sasaki, H. Kato, A. Kudo, J. Am. Chem. Soc. 135 (2013) 5441–5449.
[23] T. Peng, X. Zhang, P. Zeng, K. Li, X. Zhang, X. Li, J. Catal. 303 (2013) 156–163.
[24] X. Wang, K. Wang, K. Feng, F. Chen, H. Yu, J. Yu, J. Mol. Catal. A. 391 (2014) 92–98.
[25] X. Wang, R. Yu, P. Wang, F. Chen, H. Yu, Appl. Sur. Sci. 351 (2015) 66–73.
[26] M. Li, K. Chang, T. Wang, L. Liu, H. Zhang, P. Li, J. Ye, J. Mater. Chem. A. 3 (2015) 13731–13737.
[27] T.K. Townsend, N.D. Browning, F.E. Osterloh, Energy Environ. Sci. 5 (2012) 9543–9550.
[28] M. Liu, R. Inde, M. Nishikawa, X. Qiu, D. Atarashi, E. Sakai, Y. Nosaka, K. Hashimoto, M. Miyauchi, ACS Nano 8 (2014) 7229–7238.
[29] M. Dallavalle, N. Sändig, F. Zerbetto, Langmuir 28 (2012) 7393–7400.
[30] N. Kumar, J.M. Seminario, J. Phys. Chem. C 119 (2015) 29157–29170.
[31] W. Zhu, T. Low, Y.-H. Lee, H. Wang, D.B. Farmer, J. Kong, F. Xia, P. Avouris, Nat. Commun. 5 (2014) 3087–3094.
[32] Q. Xiang, J. Yu, M. Jaroniec, J. Am. Chem. Soc. 134 (2012) 6575–6578.
[33] A.B. Laursen, S. Kegnæs, S. Dahl, I. Chorkendorff, Energy Environ. Sci. 5 (2012) 5577–5591.
[34] S. Kanda, T. Akita, M. Fujishima, H. Tada, J. Colloid Interface Sci. 354 (2011) 607–610.
[35] K. Chang, Z. Mei, T. Wang, Q. Kang, S. Ouyang, J. Ye, ACS Nano 8 (2014) 7078–7087.
[36] K. Chang, M. Li, T. Wang, S. Ouyang, P. Li, L. Liu, J. Ye, Adv. Energy Mater. 5 (2015) 1402279.
[37] Y.H. Chang, C.T. Lin, T.Y. Chen, C.L. Hsu, Y.H. Lee, W. Zhang, K.H. Wei, L.J. Li, Adv. Mater. 25 (2013) 756–760.
[38] D.J. Li, U.N. Maiti, J. Lim, D.S. Choi, W.J. Lee, Y. Oh, G.Y. Lee, S.O. Kim, Nano Lett. 14 (2014) 1228–1233.
[39] Y. Hou, A.B. Laursen, J. Zhang, G. Zhang, Y. Zhu, X. Wang, S. Dahl, I. Chorkendorff, Angew. Chem. Int. Ed. 52 (2013) 3621–3625.
[40] H. Zhao, Y. Dong, P. Jiang, H. Miao, G. Wang, J. Zhang, J. Mater. Chem. A 3 (2015) 7375–7381.
[41] Q. Li, N. Zhang, Y. Yang, G. Wang, D.H.L. Ng, Langmuir 30 (2014) 8965–8972.
[42] S.W. Hu, L.W. Yang, Y. Tian, X.L. Wei, J.W. Ding, J.X. Zhong, P.K. Chu, Appl. Catal. B: Environ. 163 (2015) 611–622.
[43] Y. Hou, Z. Wen, S. Cui, X. Guo, J. Chen, Adv. Mater. 25 (2013) 6291–6297.
[44] M.R. Gao, J.X. Liang, Y.R. Zheng, Y.F. Xu, J. Jiang, Q. Gao, J. Li, S.H. Yu, Nat. Commun. 6 (2015) 5982.
[45] M. Tang, D. Grauer, B. Lassalle-Kaiser, V. Yachandra, L. Amirav, J. Long, J. Yano, A. Alivisatos, Angew. Chem. Int. Ed. 50 (2011) 10203–10207.
[46] X. Ge, L. Chen, L. Zhang, Y. Wen, A. Hirata, M. Chen, Adv. Mater. 26 (2014) 3100–3104.
[47] Y. Chang, C. Lin, T. Chen, C. Hsu, Y. Lee, W. Zhang, K. Wei, L. Li, Adv. Mater. 25 (2013) 756–760.
[48] H. Yu, L. Xu, P. Wang, X. Wang, J. Yu, Appl. Catal. B: Environ. 144 (2014) 75–82.
[49] P. Wang, Y. Xia, P. Wu, X. Wang, H. Yu, J. Yu, J. Phys. Chem. C 118 (2014) 8891–8898.
[50] M. Liu, K. Sunada, K. Hashimoto, M. Miyauchi, J. Mater. Chem. A 3 (2015) 17312–17319.